Doping Evolution of the Fermi Surface in Single-layer Cuprates

We have performed an angle-resolved photoemission study of the single-layer high-T_c cuprate $Bi_2Sr_{2-x}La_xCuO_{6+\delta}$ (La-Bi2201) and revealed the doping evolution of the electronic structure from the lightly-doped to optimally-doped regions. We have also observed the evolution of the Fermi "arc" into the Fermi surface. This evolution can be well explained by a rigid-band-like shift of the chemical potential, but is quite different from that observed in $La_{2-x}Sr_xCuO_4$ (LSCO), where the chemical potential does not shift, yet the dispersive band and the Fermi arc/surface are formed around the Fermi level already in the lightly-doped region.

How the electronic structure of an antiferromagnetic insulator evolves into that of a superconductor with hole doping in the high-T_c cuprates has been a fundamental issue in condensed-matter physics. So far, systematic angle-resolved photoemission (ARPES) studies on $La_{2-x}Sr_xCuO_4$ (LSCO) [1, 2] and $Ca_{2-x}Na_xCuO_2Cl_2$ (Na-CCOC) [3, 4] have revealed the doping evolution of the pseudogap in the antinodal region and of the Fermi "arc" in the nodal region from the lightly-doped to underdoped regions. However, LSCO and Na-CCOC exhibit contrasting features, such as the doping level where the quasi-particle (QP) peak at the node appears, the doping dependence of the Fermi surface volume and the Fermi surface shape, and the chemical potential shift [5, 6]. In this study, therefore, we have performed an ARPES study on another single-layer cuprate system $Bi_2Sr_{2-x}La_xCuO_{6+\delta}$ (La-Bi2201), and compared the results with those for the other single-layer cuprates in order to uncover the universal versus material-dependent behaviors in the doping evolution of the electronic structure.

High quality single crystals of La-Bi2201 were grown by the floating zone method [7]. The ARPES measurements were performed at BL-28A of the PF, and also at beamline 5-4 at the Stanford Synchrotron Radiation Lightsource (SSRL), using 55 eV (KEK-PF) and 19 eV (SSRL) photon energies and at measurement temperatures of 10-15 K in ultra-high vacuum. Samples with hole concentrations p = 0.12 – 0.18 were measured at KEK-PF and samples with p = 0.05 – 0.12 were measured at SSRL.

In Figs. 1(a)-1(c), the spectral weight at E_F is plotted in k space for each doping level, showing the evolution of the Fermi arc into the Fermi surface with hole doping. A set of Fermi momenta k_F, which define the (underlying) Fermi surface, has been determined from the peak positions of the momentum distribution curves. Figure 1(d) summarizes the doping evolution of the (underlying) Fermi surface. For the insulating p = 0.05, one can see a tiny intensity around the node. For further hole doping, the actual Fermi arc, where the QP peak crosses E_F,

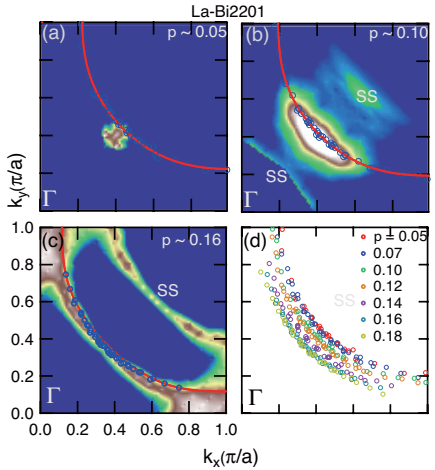

Figure 1
Doping dependence of the (underlying) Fermi surface in La-Bi2201. (a)-(c) k-space mapping of spectral weight at an E_F ±30 meV window from lightly-doped to optimally-doped La-Bi2201. Super structures due to the Bi-O modulation are labelled SS. The open blue circles indicate the k_F positions determined from the peak positions of the MDC's. The red curves show the results of tight-binding fits. (d) Doping dependence of the k_F positions, i.e., of the (underlying) Fermi surface.

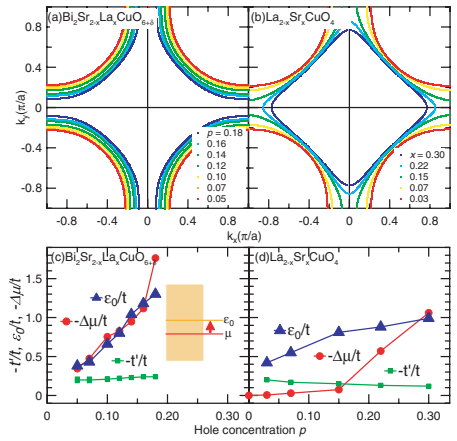

Figure 2
Doping dependence of the electronic structure in La-Bi2201 and LSCO. (a,b) Doping dependence of the (underlying) Fermi surface shape. That for LSCO has been taken from Ref.2. (c,d) Doping dependence of the tight-binding parameters t, t' and ε_0, (see text for definitions) and the chemical potential $\Delta\mu$. The parameters for LSCO are taken from Refs.2 and 6. The inset to panel (c) shows the definition of ε_0.

appears around the node at p = 0.10, and the arc length becomes longer with hole doping. In LSCO, a distinct Fermi arc with the E_F crossing of the QP peak appears already in the lightly doped non-superconducting x = 0.03 sample [1], differing from the present results, which are more similar to those of Na-CCOC [4]. The Fermi arc shape is less diamond-like than that of LSCO. The Fermi surface volume increases rapidly with doping and deviates from Luttinger's sum rule, unlike LSCO [2].

In order to evaluate the doping evolution quantitatively, we have fitted the Fermi surface shape to the two-dimensional single-band tight-binding model

$$\varepsilon_k - \mu = -2t[\cos(k_x a) + \cos(k_y a)] - 4t' \cos(k_x a)\cos(k_y a) - 2t''[\cos(2k_x a) + \cos(2k_y a)] + \varepsilon_0,$$

and compared the results with those of LSCO [2]. Here, t and t' are the nearest-neighbor and next-nearest-neighbor hopping parameters between Cu sites. The fitted (underlying) Fermi surfaces are drawn in Figs. 2(a) and 2(b). The doping dependencies of the fitted parameters are shown and compared with those of LSCO [2] in Figs. 2(c) and 2(d). The doping dependence of the chemical potential $\Delta\mu$ is determined from core-level photoemission spectra [6, 8]. The larger t' for La-Bi2201 makes the Fermi surface shape less diamond like, and the smaller t' for LSCO makes it more diamond-like. For La-Bi2201, both $-\Delta\mu/t$ and ε_0/t rapidly become larger, which means that the evolution of the electronic structure is rigid-band-like. On the other hand, for LSCO, $-\Delta\mu/t$ and ε_0/t show different doping dependencies. Effects due to crystal structure disorder may affect the doping evolution and T_c. The material-dependent doping evolution may also be related to the electronic structure ordering.

REFERENCES

[1] T. Yoshida, X.J. Zhou, T. Sasagawa, W.L. Yang, P.V. Bogdanov, A. Lanzara, Z. Hussain, T. Mizokawa, A. Fujimori, H. Eisaki, Z.-X. Shen, T. Kakeshita and S. Uchida, *Phys. Rev. Lett.*, **91** (2003) 027001.
[2] T. Yoshida, X.J. Zhou, D.H. Lu, S. Komiya, Y. Ando, H. Eisaki, T. Kakeshita, S. Uchida, Z. Hussain, Z.-X. Shen and A. Fujimori, *J. Phys.: Condens. Matter*, **19** (2007) 125209.
[3] K.M. Shen, F. Ronning, D.H. Lu, W.S. Lee, N.J.C. Ingle, W. Meevasana, F. Baumberger, A. Damascelli, N.P. Armitage, L.L. Miller, Y. Kohsaka, M. Azuma, M. Takano, H. Takagi and Z.-X. Shen, *Phys. Rev. Lett.*, **93** (2004) 267002.
[4] K.M. Shen, F. Ronning, D.H. Lu, F. Baumberger, N.J.C. Ingle, W.S. Lee, W. Meevasana, Y. Kohsaka, M. Azuma, M. Takano, H. Takagi and Z.-X. Shen, *Science*, **307** (2005) 5011.
[5] H. Yagi, T. Yoshida, A. Fujimori, Y. Kohsaka, M. Misawa, T. Sasagawa, H. Takagi, M. Azuma and M. Takano, *Phys. Rev. B*, **73** (2006) 172503.
[6] A. Ino, T. Mizokawa, A. Fujimori, K. Tamasaku, H. Eisaki, S. Uchida, T. Kimura, T. Sasagawa and K. Kishio, *Phys. Rev. Lett.*, **79** (1997) 2101.
[7] S. Ono and Y. Ando, *Phys. Rev. B*, **67** (2003) 104512.
[8] M. Hashimoto, T. Yoshida, H. Yagi, M. Takizawa, A. Fujimori, M. Kubota, K. Ono, K. Tanaka, D.H. Lu, Z.-X. Shen, S. Ono and Y. Ando, *Phys. Rev. B*, **77** (2008) 094516.

BEAMLINE

28A

M. Hashimoto[1], T. Yoshida[1], A. Fujimori[1], M. Kubota[2], K. Ono[2], K. Tanaka[3], D.H. Lu[3], Z.-X. Shen[3], S. Ono[4], Y. Ando[5] ([1]The Univ. of Tokyo, [2]KEK-PF, [3]Stanford Univ., [4]CRIEPI, [5]Osaka Univ.)

Functional Carbon Nanotubes Filled with Water

Single-wall carbon nanotubes (SWNTs) have cylindrical cavities with diameters of 8 to 20 Å, in which many kinds of molecules can be encapsulated. Although the walls are made up of a hydrophobic graphite layer, it is known that water can also easily be encapsulated within the cavities. Recently, further examinations on water stability inside SWNTs have been conducted, and it has been clarified that a new type of phase transition occurs at low temperature under atmospheric (gaseous) conditions. The transition is ascribed to an exchange phenomenon between water and atmospheric gas molecules. On the basis of this phenomenon, it is proposed that water-SWNTs are used to fabricate new types of gas-selective molecular nano-valves and gas sensors.

Single-wall carbon nanotubes (SWNTs) with one-dimensional cavities of diameter 8 to 20 Å are made with a single graphite layer. They are able to encapsulate many kinds of molecules within their cavities. Such encapsulations often lead to substantial changes in physical properties. Water is one of the molecules which can be encapsulated. In spite of the hydrophobic nature of the graphite wall, SWNTs easily adsorb water following heat treatment in air. The water inside the SWNTs undergoes novel liquid-solid phase transitions, in which the low temperature solid-like structures are assigned to so-called ice-nanotubes [1-3], as schematically shown in Fig. 1. Recently, further investigations on water-SWNTs have been performed in gas-atmospheric conditions by means of X-ray diffraction, NMR, electrical resistivity, and molecular dynamics (MD) calculations [4]. It was discovered that a new type of phase transition occurs at low temperatures in gas-atmosphere. This observation suggests new applications for water-SWNT composites such as gas-selective molecular nano-valves and gas sensors.

Figure 2 shows the temperature (T) dependence of the electrical resistivity of water-filled SWNT films in various gas atmospheres at 1 atm. SWNTs with an average diameter of 13.5 Å were used, following heat-treatment in air to open them. It is found that the resistivity exhibits a significant increase below a critical temperature T_c, shown by an arrow in Fig. 2. Further measurements reveal that T_c depends on not only the species of the gas molecules but also on the gas pressure. On the basis of this phenomenon, it is proposed that water-SWNTs are used to fabricate a new type of gas sensor.

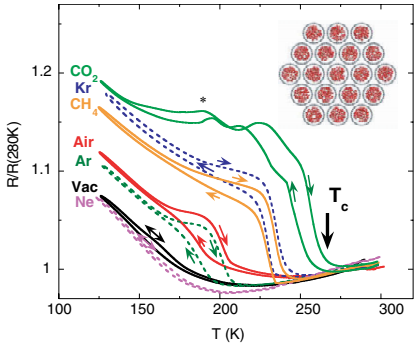

Figure 2
Temperature dependence of the electrical resistivity of a water-filled SWNT film in various gas atmospheres at 1 atm. The arrow shows the critical temperature for CO_2. Inset: a schematic illustration of a bundle of SWNTs filled with water.

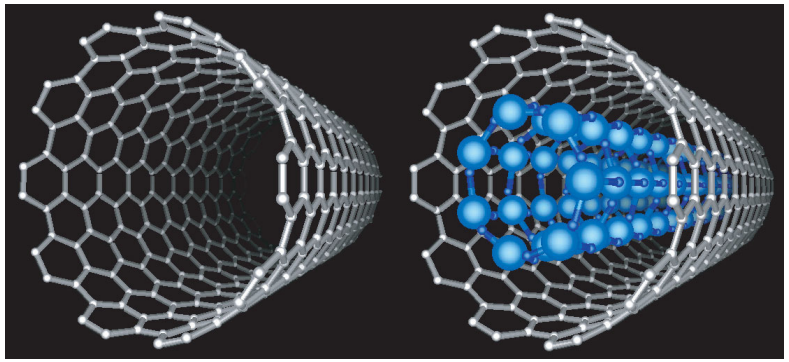

Figure 1
Schematic illustrations of a single-wall carbon nanotube (left) and a heptagonal ice nanotube (right). The blue spheres represent the water oxygen atoms, and the hydrogen atoms are not shown.

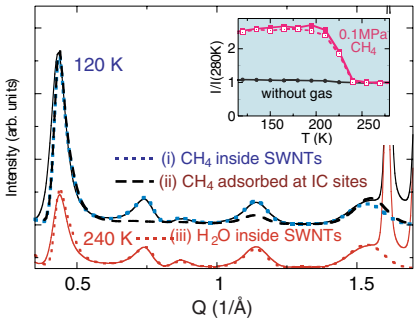

Figure 3
X-ray diffraction patterns of water-filled SWNTs in a CH_4 atmosphere at 1 atm below and above T_c. The dotted and dashed lines are the calculated patterns. The best fits indicate that some water molecules are ejected from the SWNTs below 240 K. The calculations give no evidence for the adsorption of CH_4 molecules at the interstitial channels (IC) which are surrounded by three SWNTs in the bundles. The inset shows the temperature dependence of the intensity of the Bragg peak at $Q \approx 0.4$ Å^{-1}.

To clarify the origin of the observed transition, X-ray diffraction (XRD) structural analysis was conducted at BL-1B using X-ray radiation with a wavelength of 1.00 Å. Figure 3 shows examples of the XRD patterns taken below and above T_c ~240 K for the case of methane (CH_4) at 1 atm. Detailed analysis of the patterns reveals that water is ejected from the inside of the SWNTs below T_c. Combined with additional information obtained from ^{1}H-NMR measurements of CH_4 in D_2O-filled SWNTs, it is concluded that below T_c CH_4 molecules enter the SWNTs and push out the water molecules in an on-off fashion. The transition is thus attributed to an exchange phenomenon between the water molecules inside the SWNTs and the atmospheric gas molecules. The transition is assumed to be caused by a competition between water-SWNT and gas-SWNT interactions, and thus one of atomic scale phenomena. Furthermore, it is proposed from the MD calculations that water-SWNTs have a potential application as molecular-selective nano-valves [4].

REFERENCES

[1] Y. Maniwa, H. Kataura, M. Abe, S. Suzuki, Y. Achiba, H. Kira and K. Matsuda, *J. Phys. Soc. Jpn.*, **71** (2002) 2863.
[2] Y. Maniwa, H. Kataura, M. Abe, A. Udaka, S. Suzuki, Y. Achiba, H. Kira, K. Matsuda, H. Kadowaki and Y. Okabe, *Chem. Phys. Lett.*, **401** (2005) 534.
[3] K. Koga, G.T. Gao, H. Tanaka and X.C. Zeng, *Nature,* **412** (2001) 802.
[4] Y. Maniwa, K. Matsuda, H. Kyakuno, S. Ogasawara, T. Hibi, H. Kadowaki, S. Suzuki, Y. Achiba and H. Kataura, *Nature Materials,* **6** (2007) 135.

BEAMLINE

1B

Y. Maniwa[1,2], K. Matsuda[1], H. Kyakuno[1], S. Ogasawara[1], T. Hibi[1], S. Suzuki[1], Y. Achiba[1], H. Kadowaki[1], H. Kataura[2,3] ([1]Tokyo Metropolitan Univ., [2]CREST [3]National Inst. of Adv. Indus. Sci. and Tech.,)

Structural Study on the Origin of Polarization in Hydrogen-bonded Supramolecular Ferroelectrics

Ferroelectric transitions are seen in a 1:1 adduct of phenazine with chloranilic acid and bromanilic acid, in which nonpolar neutral molecules are connected by intermolecular O-H···N hydrogen bonds. A maximum entropy method (MEM) analysis of synchrotron X-ray diffraction data reveals two inequivalent hydrogen-bonding sites below the ferroelectric transition temperature (253 K for Phz-H_2ca, 168 K for Phz-H_2ba). The asymmetry is also observed in a neutron diffraction analysis, and the results suggest that the origin of the polarization of the material is symmetry breaking based on the two inequivalent hydrogen bonds.

Studies on ferroelectrics have been motivated by interests not only in basic science but also in application to electronics. Recently we have developed new ferroelectric organic solids with supra-molecular structures; the co-crystals of phenazine (Phz) with chloranilic acid (H_2ca) and bromanilic acid (H_2ba), in which non-polar neutral molecules are connected by intermolecular O-H···N hydrogen bonds (H-bonds) [1, 2]. The Phz-H_2ca crystal shows a large dielectric constant around the Curie temperature Tc_1, which is as high as 253 K. In crystals of Phz-H_2xa (x = c, b), the observed polarizations are much higher than values calculated using a molecular dipole model. Therefore, the H-bond (and/or the proton dynamics) is anticipated to play an important role in the appearance of spontaneous polarization. In this paper, we report the electron density distribution obtained from synchrotron X-ray diffraction analysis, and a crystal structure analysis of neutron diffraction data, in an attempt to pursue the origin of the polarization.

The single crystals for the diffraction studies were grown using standard methods. The X-ray diffraction measurements were performed using monochromatized synchrotron X-rays and the imaging plate system installed at BL-1A. The neutron diffraction experiments were performed at the T2-2 guide-hall of JRR-3 at the Japan Atomic Energy Agency, utilizing the four-circle diffractometer FONDER.

In X-ray diffraction analysis, it is generally difficult to specifically locate the electron density of the lightest element H using conventional least-square refinement. In order to probe small changes, we calculated the electron-density distribution using the maximum entropy method (MEM). Figure 1(a) shows the three-dimensional map of electron density obtained from the MEM analysis of the synchrotron radiation X-ray diffraction data of Phz-H_2ca at 160 K. In the ferroelectric phase there are two crystallographically independent OH···N H-bond sites. From the electron-density contour plot of

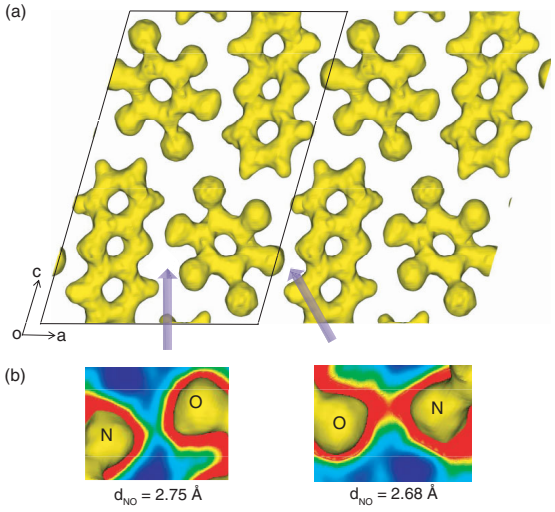

Figure 1
(a) Electron-density distribution map obtained by maximum entropy method (MEM) analysis of the X-ray diffraction data of Phz-H_2ca at 160K. The equi-contour level is at 0.7 eÅ^{-3}. (b) Contour map of the electron density near the H-bonding OH···N site extracted on the plane defined by two oxygen atoms and one nitrogen atom. The contour maps are drawn from 0 eÅ^{-3} (blue) to 0.4 eÅ^{-3}(red).

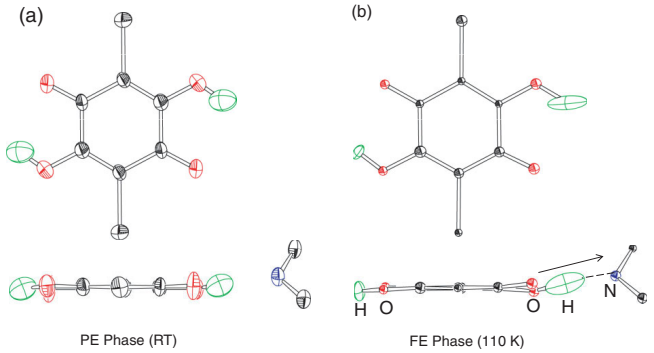

Figure 2
Molecular structure of H_2ba in the (a) paraelectric (T = 300 K) and (b) ferroelectric (110 K) phases obtained from the neutron diffraction analysis. Each structure is represented by thermal ellipsoids at the 50% probability level.

the OH···N site (Fig 1(b)), one can find the difference of the electron density distribution between the two H-bond sites. In the shorter N···O site (d_{NO} = 2.68 Å, right panel of Fig. 1(b)), a more delocalized electron density can be observed than in the longer N···O site (d_{NO} = 2.75 Å, left panel of Fig. 1(b)). The inequivalence of the two H-bond sites which suggests a symmetry-breaking displacement of hydrogen may be the origin of the ferroelectricity of this material. The hydrogen delocalization and simultaneous deformation of the H-bonds also implies the incipient character of the proton-transferred N-H$^+$···O$^-$ form, breaking the crystal inversion symmetry and generating the spontaneous polarization.

Such delocalization and asymmetry of the electron-density distribution at the two H-bonding sites is also observed in the neutron diffraction analysis. Figure 2 shows the molecular structure of the paraelectric (Fig. 2(a), RT) and ferroelectric (Fig. 2(b), 110K) phases of H_2ba in the Phz-H_2ba crystal obtained from the neutron crystal structure analysis. For both the Phz-H_2xa co-crystals, the lattice parameters, space group ($P2_1$), and atomic coordinates (except for H atoms), agree with those obtained from the X-ray diffraction experiments. All the H-bonds appear to be O-H···N type even in the ferroelectric phase, confirming the neutral nature of the molecules. The paraelectric phase structure (Fig. 2a) exhibits the symmetric (nonpolar) molecular structure of H_2ba without any hydrogen disorder. On the other hand, a significantly elongated thermal ellipsoid of one H nuclei in the low-temperature FE phase is observed (Fig. 2(b)), indicating an asymmetric structure with a broadly-distributed H atom. This broadly-distributed H atom corresponds to the H-bond site which shows delocalized electron density in the MEM analysis (Fig. 1(b)). The delocalized H atom deviates from the π-skeleton plane of H_2ba, and is displaced toward the nitrogen atom of the neighboring Phz molecule, lying out of the H_2ba molecular plane. The broadly-distributed H nucleus approaches the center point in the strengthened O-H···N bond. Very similar molecular structures are also observed in the Phz-H_2ca crystal.

The present diffraction study reveals the symmetry-breaking displacement of H atoms in the emergence of ferroelectricity in organic supramolecules. The similar proton affinity of the acid and bases seemingly reduces the potential barrier for H to move toward the base, allowing large displacing deformations. The resultant asymmetry of the H-bonds is the origin of the dipole moment. The structural study shows that the H-bond plays an essential role in producing the polarization in this system.

REFERENCES

[1] S. Horiuchi, F. Ishii, R. Kumai, Y. Okimoto, H. Tachibana, N. Nagaosa and Y. Tokura, *Nature Mat.*, **4** (2005) 163.
[2] S. Horiuchi, R. Kumai and Y. Tokura, *J. Am. Chem. Soc.*, **127** (2005) 5010.

BEAMLINE

1A

R. Kumai[1], S. Horiuchi[1], H. Sagayama[2], T. Arima[2], M. Watanabe[2], Y. Noda[2] and Y. Tokura[1,3,4] ([1]AIST-CERC, [2]Tohoku Univ., [3]ERATO-MF, [4]The Univ. of Tokyo)

Domain Formation in the Organic Superconductor κ_L-(DMEDO-TSeF)$_2$[Au(CN)$_4$](THF)

The structural properties of the disordered organic superconductor κ_L-(DMEDO-TSeF)$_2$[Au(CN)$_4$](THF) have been investigated. Here DMEDO-TSeF and THF represent dimethyl(ethylenedioxy)tetraselenafulvalene and tetrahydrofuran, respectively. We have found that an orthorhombic-monoclinic distortional phase transition occurs at T_d = 209 K, where the *b*-axis tilts by 1.2° in the *bc*-plane. The low-temperature structure is composed of two monoclinic domains with the space group $P2_1/n11$. The low-temperature phase has two crystallographically independent dimers in a conducting layer composed of the donor molecules, suggesting that the present compound potentially borders on the charge ordered state, and has possibly different symmetry of superconductivity from ordinary κ-type superconductors.

Most organic superconductors are clean single crystals, i.e., the donor molecules and anions are in ordered states. By contrast, the recently synthesized organic superconductor κ_L-(DMEDO-TSeF)$_2$[Au(CN)$_4$](THF) (Fig. 1(a)) has disordered solvent molecules THF [1]. We have studied the structural properties of this compound in order to clarify how the disorder affects the superconductivity.

Single crystals were prepared by electrocrystallization at RIKEN [1]. The X-ray oscillation photographs were taken with 11.0 keV synchrotron radiation using an imaging plate diffractometer installed at BL-1B. Twin structure was measured on a four-circle diffractometer with graphite monochromated Mo-$K\alpha$ radiation at Tokyo Institute of Technology. The sample temperature was controlled by a nitrogen gas-stream cooling system.

The X-ray oscillation photographs are shown in Fig. 1(b). The single Bragg spot splits into two at 200 K, and this splitting recovers to a single spot at 220 K. Figures 1(c) and (d) show the peak profiles at 291 K and 110 K. A clear peak splitting is observed in the (0 0 2) reflection only along the b^*-axis of the prototype lattice. The splitting does not occur in either the (0 *k* 0) or (*h* 0 0) reflections along either of the two vertical axes. These observations show that the *b*-axis tilts in the *bc*-plane of the prototype lattice in real space, and that the low-temperature structure is composed of two monoclinic domains. The distortion angle δ defined as $\delta = |\alpha - 90°|$ is estimated to be 1.21(2)° at 110 K. The integrated intensity ratio of domain 1 to domain 2 directly gives the volume ratio of the two domains, and is almost 1:1. The distortion angle δ is zero at the orthorhombic-monoclinic distortion temperature, T_d = 209 K.

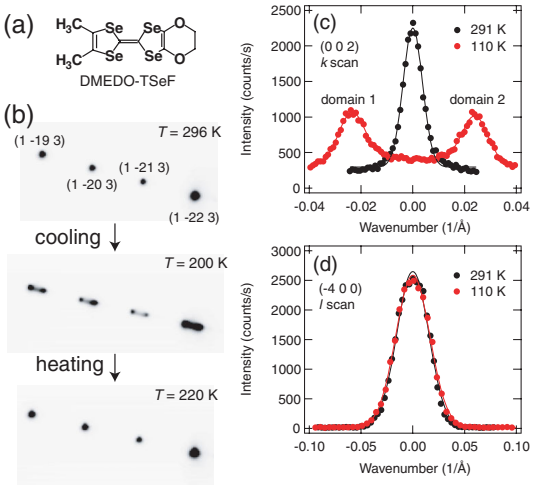

Figure 1
(a) DMEDO-TSeF molecule, (b) X-ray oscillation photographs, and (c) and (d) high- and low-temperature peak profiles.

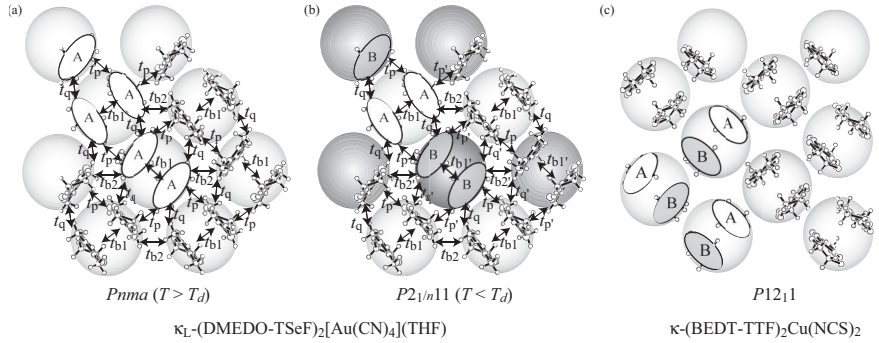

Figure 2
Schematic drawing of the donor arrangement both at (a) $T > T_d$ and at (b) $T < T_d$, and (c) that of κ-(BEDT-TTF)$_2$Cu(NCS)$_2$. Shaded circles represent dimers.

The low-temperature space group is found to be $P2_1/n11$ from the number of variants and the peak profiles based on group-theoretical consideration [2,3]. The possible domain wall is parallel to the *ac*-plane of the prototype lattice based on Sapriel's theory and the peak profiles at 110 K [4].

In the high temperature orthorhombic phase of the present compound, there is only one crystallographically independent donor molecule, the A molecule, as shown in Fig. 2(a). By contrast, the low-temperature phase has two crystallographically independent donor molecules, A and B in Fig. 2(b), within each donor layer, and there are two independent dimers, the A-A and B-B pairs in the conducting layer. This structure differs from the organic superconductor κ-(BEDT-TTF)$_2$Cu(NCS)$_2$ [BEDT-TTF: bis(ethylenedithio)tetrathiafulvalene], which is composed of one crystallographically independent dimer, as shown in Fig. 2(c). All κ-type BEDT-TTF superconductors ever reported have the structures shown in panels (a) or (c), composed of only one crystallographyically independent dimer, and the superconducting phase borders on the antiferromagnetic Mott insulating state in the temperature-pressure phase diagram, the so-called Kanoda diagram [5]. On the other hand, the panel (b) type structure has been reported in another insulating state, charge ordered BEDT-TTF salts [6]. This structure potentially shows charge order, because the valence of the molecule A is not necessarily identical to that of B. Only the present compound shows superconductivity in spite of having a panel (b) type structure. This suggests that the origin and symmetry of the superconductivity of the present compound differ from those of the usual κ-type superconductors [7].

REFERENCES

[1] T. Shirahata, M. Kibune and T. Imakubo, *Chem. Commun.*, (2006) 1592.
[2] G.Van Tendeloo and S. Amelinckx, *Acta Crystallogr. A*, **30** (1974) 431.
[3] V. Janovec, V. Dvorak and J. Petzelt, *Czech. J. Phys. B*, **25** (1975) 1362.
[4] J. Sapriel, *Phys. Rev. B*, **12** (1975) 5128.
[5] K. Kanoda, *Hyperfine Interact.*, **104** (1997) 235.
[6] A. Ota, L. Ouahab, S. Golhen, Y. Yoshida, M. Maesato, G. Saito and R. Swietlik, *Chem. Mater.*, **19** (2007) 2455.
[7] T. Kawamoto, T. Mori, T. Kakiuchi, H. Sawa, T. Shirahata, M. Kibune, H. Yoshino and T. Imakubo, *Phys. Rev. B*, **76** (2007) 134517.

BEAMLINE

1B

T. Kawamoto[1], T. Mori[1], T. Kakiuchi[2], H. Sawa[2], T. Shirahata[3], M. Kibune[3], H. Yoshino[3], T. Imakubo[3]
([1]Tokyo Inst. of Tech., [2]KEK-PF, [3]RIKEN)

Extended X-Ray Absorption Fine Structure Study of Tellurium Nanoparticles

The structure of tellurium nanoparticles was studied by extended X-ray absorption fine structure measurements. The twofold coordinated chains which characterize trigonal tellurium (t-Te) are preserved even in the nanoparticles, but the covalent bonds (intrachain interactions) are stronger than those of t-Te, as shown by a shorter bond length and higher Einstein temperature. The interchain interactions are weakened, as shown by a 50% decrease in interchain coordination number compared to t-Te.

Nanoparticles show different physical properties and structure to those of the bulk. To date, most studies of nanoparticles have concentrated on metallic and semiconductor materials (such as Si, Ge, and CdS) [1,2]. The number of studies on materials having a secondary structure is small. The trigonal tellurium (t-Te) has a hierarchical structure consisting of helical chains of covalently bound atoms with three atoms per turn, which are bound together to form a hexagon. By contrast, the structure of Te nanoparticles is unknown, and may be exotic in nature.

The tellurium nanoparticles studied here were made by island deposition and surrounded by NaCl. The average film thickness of the Te layers was 0.5 nm. EXAFS measurements were performed in transmission mode at AR-NW10A [3].

Figure 1 shows Fourier transforms of the EXAFS functions. The first and second peaks correspond to the intrachain first nearest neighbor (1NN) and the interchain 1NN distances, respectively. The third peak is assigned to contributions from the second nearest neighbor (2NN) distances of the intra- and interchain.

Structural parameters for the intra- and interchain 1NN atoms are given in Table 1. The coordination number for the intrachain 1NN of the nanoparticles is close to that of t-Te, suggesting that the primary structure is preserved. The most interesting features observed for the nanoparticles are the shortening of the covalent bonds and the preservation of the 1NN coordination number within the chains. The intrachain bond distance of the nanoparticles is 0.042 Å shorter than that of t-Te. Following an empirical relation between covalent bond length and force constant [4], the force constant of the nanoparticles is about 1.1 times larger than that of t-Te.

Figure 2 shows the temperature dependence of the Debye-Waller factor σ^2 for the intrachain 1NNs, from which the Einstein temperatures Θ_E are obtained (see Table 1). The value of Θ_E for the nanoparticles is higher than that for t-Te. In the harmonic oscillator approximation, this leads to the force constant for the nanoparticles 1.3 times larger than that for t-Te, the result comparable to that obtained from analysis of the covalent bond length.

The average coordination number for the interchain 1NN of the nanoparticles is about half that of t-Te, indicating that the interchain interactions are reduced in the nanoparticles. Since hybridization between the lone-pair orbitals and the anti-bonding orbitals in the adjacent chains weakens the intrachain covalent bond, the reduction of the interchain interactions induces the covalent bond shrinkage and the enhancement of the force constant in the nanoparticles.

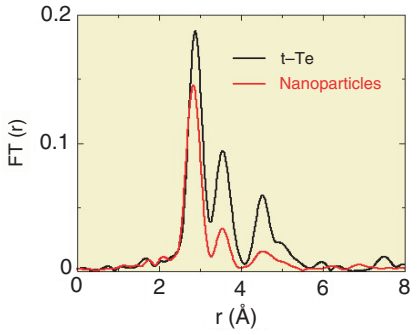

Figure 1
Fourier transform magnitude of the EXAFS $k\chi(k)$ data measured at 20 K for t-Te and the nanoparticles.

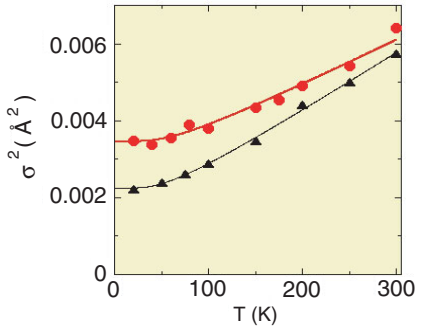

Figure 2
Debye-Waller factor of the intrachain nearest neighbor for t-Te (black triangles) and nanoparticles (red circles) as a function of measurement temperature, along with the correlated Einstein model fits (solid lines).

Table 1
Structural parameters (bond length r, coordination number N and Einstein temperature Θ_E) obtained from the best fits to the EXAFS experimental spectra for t-Te and the nanoparticles. Statistical calculations were performed below 100 K.

		Intrachain		Interchain
	r (Å)	N	Θ_E (K)	N
t-Te	2.834±0.002	2.00±0.05	157	4.25±0.30
Nanoparticles	2.792±0.001	1.94±0.03	178	2.17±0.31

In summary, Te nanoparticles have the following important characteristics compared to t-Te: the existence of a covalently-bonded chain structure; shrinkage of the bonds; an increase in the force constant for the intrachain 1NN; and a decrease in interchain interactions. The twofold-coordinated covalent bonds are similar to those of t-Te and the chain structure is preserved, whereas the interchain interactions are reduced because they are weaker than the intrachain interactions. The covalent bond shrinkage is caused by the decrease in the overlap between orbitals in adjacent chains together with the weakening of the interchain interactions.

REFERENCES

[1] C. Burda, X. Chen, R. Narayanan and M.A. El-Sayed, *Chem. Rev.*, **105** (2005) 1025.
[2] T. Trindade, P. O'Brien and N.L. Pickett, *Chem. Mater.*, **13** (2001) 3843.
[3] H. Ikemoto and T. Miyanaga, *Phys. Rev. Lett.*, **99** (2007) 165503
[4] G.R. Freeman and N.H. March, *J. Mol. Struct.(Theochem)*, **333** (1995) 261.

BEAMLINE

AR-NW10A

H. Ikemoto[1] and T. Miyanaga[2] ([1]Univ. of Toyama, [2]Hirosaki Univ.)

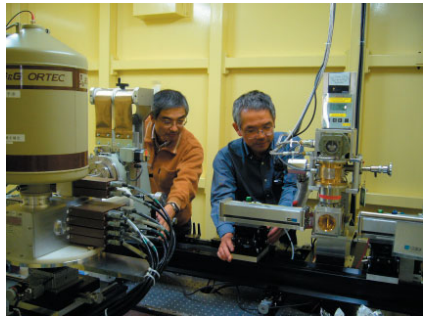

Uniaxial Lattice Deformation of CdS Single Crystal by Laser-induced Dynamical Compression

We have measured uniaxial lattice deformation of a CdS single crystal under shock-wave loading on the nanosecond time scale. The shock-wave was generated using laser ablation on the *ab*-plane of the sample surface, and travels through the crystal along the *c*-axis. The diffraction spots observed under shock-wave loading shift to higher-angles due to compression of the *c*-axis of the crystal. A transient wurtzite structure above the threshold pressure for the phase transition was directly observed at times shorter than 10 ns.

Understanding the dynamics of materials under shock compression is an essential key to understanding various impact phenomena, including meteor impact, armour penetration, and interstellar dust-dust collisions. Atomic motion and the history of atomic rearrangement under shock-waves can be studied using time-resolved Laue diffraction with high-flux white X-rays. Gupta and co-workers investigated the dynamics of the shock-induced phase transition in cadmium sulfide (CdS) from wurtzite to rocksalt structures using time-resolved absorption spectroscopy [1,2]. The initial wurtzite structure of the CdS single crystal transformed to the high-pressure phase at 3.25 GPa compression along the *c*-axis. Elastic compression along the shock loading direction changes to uniform compression at the phase transition point. We report here on the laser-induced shock response of the CdS single crystal around the pressure of the phase transition as studied using single-shot time-resolved Laue diffraction.

We have constructed 100-ps time-resolved X-ray diffraction, scattering, and absorption measurement systems at the AR-NW14A [3]. A schematic drawing is shown in Fig. 1, and the sample assembly is described in detail in ref. [4]. Laser-induced shock waves propagate through the irradiation plane to the backward plane along the *c*-axis, and parallel to the X-ray beam.

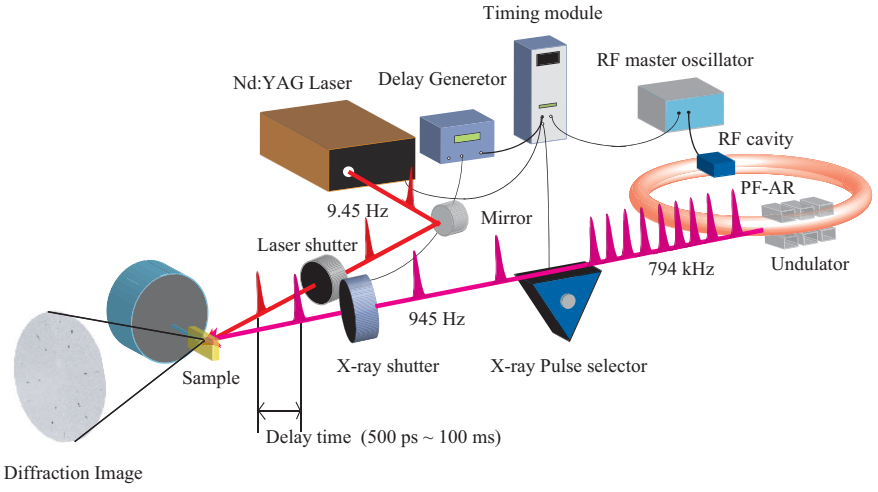

Figure 1
Experimental setup for the single-shot time-resolved Laue diffraction. The pump-laser is a Nd:YAG laser (Continuum, Powerlite8000), and the frequency ,wavelength, laser power and pulse width are 10 Hz, 1064 nm, 860 mJ, and 10 ns, respectively. The YAG laser is synchronized with the storage ring at 9.45 Hz, which is the 53,760,000th harmonic of the RF master clock (508.58 MHz). The energy bandwidth, frequency, and photon flux of the probe X-ray pulse are 15%, 945 Hz, and 10^9 photons/pulse, respectively. The delay timings between the X-ray pulse and laser pulse can be controlled using a delay generator.

Figure 2 shows a series of Laue diffraction images recorded during shock wave loading (Fig. 2(a)), and also plots of the diffraction intensity as a function of the 2θ angle along the directions of the (201) and (302) peaks (Fig. 2(b)). The peaks on the Laue images initially move to higher 2θ angle, then return to their original positions after around 22 ns. These shifts clearly indicate the occurrence of anisotropic compression. The shock wave arrives at the backward plane after around 12 ns, then reflects towards the irradiation plane, arriving after around 22 ns, as shown in Fig. 2(b). The broadening of the peaks at 22 ns shows the residual stress due to the shock loading. These results allow us to estimate the shock wave speed to be 4.2±0.5 km/s, which is in good agreement with the elastic velocity. The shift of the peak position depends on the change of the lattice constant ratio, *c/a*. The 2θ angle of the (201) peak at 15 ns is 31.24°, which corresponds to a 4.4% decrease in the *c/a* ratio. If we assume the shock compression to be purely uniaxial, the shock pressure can be estimated to be 3.92 GPa for 4.4% compression from the elastic region, as shown in Fig. 2 (c). This is higher than the threshold pressure of the phase transition (~ 3 GPa), however the retention time of the shock-compressed condition using this method (~ 10 ns) is shorter than the incubation time required for the phase transition from wurtzite-to-rocksalt structures. Thus, in this study, a transient CdS structure beyond the shock-induced phase transition pressure is clearly captured using single-shot time-resolved Laue diffraction. Our method will become a powerful tool for revealing the detailed ultrafast dynamics of single crystals under shock-wave loading.

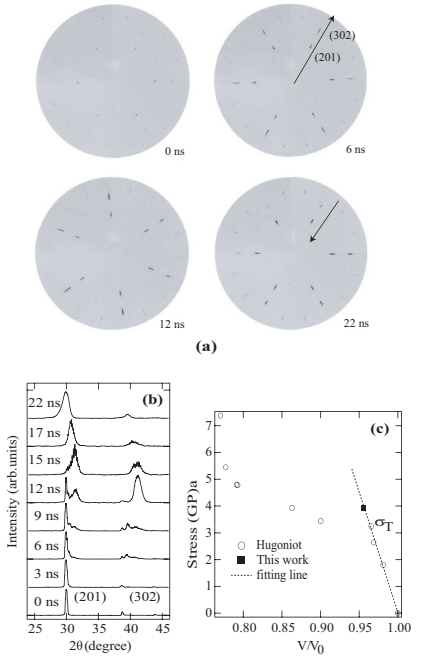

Figure 2
(a) Time-resolved Laue diffraction of the CdS single crystal. The images at each delay were recorded by single-shot exposure. (b) (201) and (302) peaks on the six-folding axis from the time-resolved Laue images. The peaks shift to higher angles before moving back to their original positions, due to the shock loading. (c) Stress-volume plane for the CdS single crystal. δ_T is the phase transition point at 3.25 GPa. The circles are the Hugoniot data for the CdS crystal, and the filled square is the results obtained in this study. The dotted line is a smooth fit in the elastic region.

REFERENCES

[1] M.D. Kundson, Y.M. Gupta and A.B. Kunz. *Phys. Rev. B.*, **59** (1999) 11704.
[2] M.D. Kundson and Y.M. Gupta. *J. Appl. Phys.*, **91** (2002) 9561.
[3] S. Nozawa, S. Adachi, J. Takahashi, R. Tazaki, L. Guerin, M. Daimon, A. Tomita, T. Sato, M. Chollet. H. Cailleau, S. Yamamoto, K. Tsuchiya, T. Shioya, H. Sasaki, T. Mori, K. Ichiyanagi, H. Sawa, H. Kawata and S. Koshihara. *J. Synchrotron. Rad.*, **14** (2007) 313.
[4] K. Ichiyanagi, S. Adachi, S. Nozawa, Y. Hironaka, K.G. Nakamura, T. Sato, A. Tomita and S. Koshihara. *Appl. Phys. Lett.*, **91** (2007) 231918.

BEAMLINE

AR-NW14A

K. Ichiyanagi[1], T. Sato[1, 2], S. Nozawa[1], A. Tomita[1, 2], Y. Hironaka[3], K.G. Nakamura[4], S. Adachi[1, 5] and S. Koshihara[1,2] ([1]ERATO-JST, [2]Titech, [3]Univ. of Osaka, [4]MSL Titech, [5]KEK-PF)

Crystallization Behavior of Poly(δ-valerolactone) Homopolymers Confined in Isolated Nanodomains

The isothermal crystallization of poly(δ-valerolactone) (PVL) homopolymers ([-$(CH_2)_4$-CO-O-]$_n$) spatially confined in isolated nanodomains surrounded by polystyrene (PS) matrices has been investigated using differential scanning calorimetry (DSC) and synchrotron small-angle X-ray scattering (SR-SAXS). The samples were prepared by the microphase separation of PVL-*b*-PS copolymers followed by photocleavage at block junctions. The crystallinity and melting temperature of the PVL homopolymers were found to be significantly higher than those of PVL blocks, *i.e.*, PVL with one chain-end tethered at the nanodomain interface. However, the initial crystallization rate of the PVL blocks was observed to be significantly higher than that of the PVL homopolymers under identical crystallization conditions, indicating the dominance of nucleation at the interface.

The crystallization of block copolymers provides an interesting research subject from the viewpoint of nanostructure control in polymer materials. It is well known that isolated nanodomains (*i.e.*, cylinders or spheres) affect the crystallization of constituent blocks resulting in a considerable decrease in crystallization temperature T_c and crystallinity [1]. Two restrictions are expected to simultaneously affect the crystallization behavior ((**a**) in Fig. 1(A)): (1) *spatial confinement* by nanodomains surrounding the crystalline blocks and (2) *chain confinement* by tethering at the nanodomain interface. To understand these effects separately it is necessary to prepare a system where crystalline homopolymers are confined in isolated nanodomains (**b**) and to investigate the difference in crystallization behavior between two systems (**a**/**b** or **b**/**c**). Here we report on the difference in crystallization behavior between PVL blocks and PVL homopolymers both confined in PS nanodomains [2].

We synthesized two PVL-*b*-PS copolymers (with PVL volume fractions ϕ_{PVL} of 0.29 and 0.12) with photocleavable groups between different blocks. The vitrification of the PS chains prevents the macroscopic phase separation between PVL and PS homopolymers after photocleavage, and eventually we can observe crystallization of the PVL homopolymers confined in the PS nanodomains originally formed by microphase separation of the PVL-*b*-PS copolymers. The microphase-separated structures were investigated using SR-SAXS at BL-10C. We also obtained the melting temperature T_m and heat of fusion ΔH (proportional to PVL crystallinity) from DSC measurements. Furthermore, ΔH was determined as a function of crystallization time to compare the crystallization behavior among the different samples.

Figure 1(B) shows the SAXS curves recorded at room temperature (where PVL is crystallized) and at 70°C (PVL is melted) for PVL-*b*-PS with ϕ_{PVL} = 0.29 before (PVL-PS) and after (PVL/PS) photocleavage. The room temperature curves show some scattering peaks, the positions of which exactly correspond to a ratio of 1:$\sqrt{3}$:$\sqrt{4}$, indicating the formation of PVL cylindrical nanodomains. The SAXS curves recorded at 70°C show a similar pattern, with the primary peak position unchanged. The SAXS curves for PVL-*b*-PS with ϕ_{PVL} = 0.12 revealed spherical nanodomains, which again did not change at 70°C. These results indicate clearly that cylindrical and spherical nanodomains are completely preserved in PVL/PS even after melting of the PVL homopolymer, and therefore that it is possible to investigate the difference in crystallization behavior between PVL blocks (Fig. 1(A), (a)) and PVL homopolymers (Fig. 1(A), (b)) with identical spatial confinement.

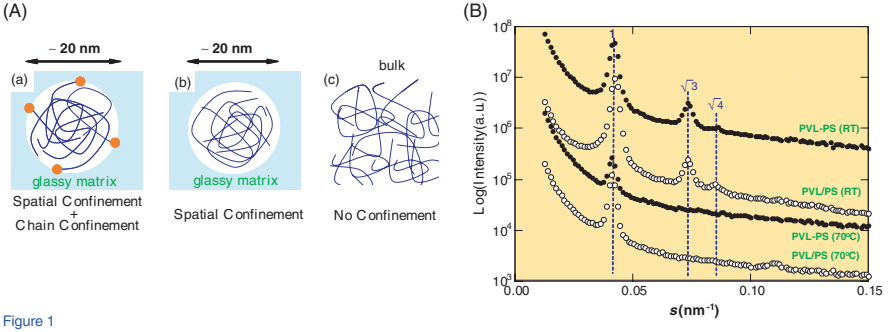

Figure 1
(A) Schematic illustration showing crystalline blocks (**a**) and crystalline homopolymers (**b**) both confined in a spherical nanodomain, and crystalline homopolymers without any confinement (**c**). (B) SR-SAXS curves for PVL-PS (closed circles) and PVL/PS (open circles) at room temperature (top two curves) and 70°C (> T_m, bottom two curves).

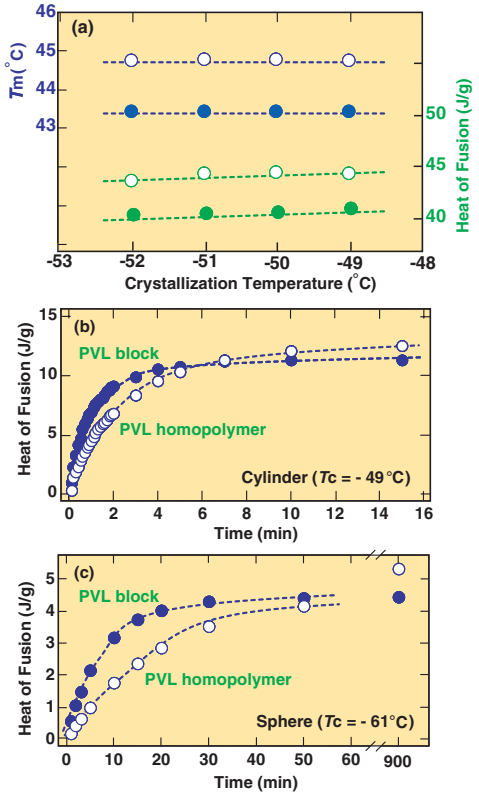

Figure 2
(**a**) T_m and ΔH per 1g of PVL plotted against T_c for PVL homopolymers (open circles) and PVL blocks (closed circles) confined in cylindrical nanodomains. (**b**, **c**) ΔH per 1g of sample plotted against crystallization time for PVL homopolymer (open circles) and PVL blocks (closed circles) confined in cylindrical (**b**) and spherical (**c**) nanodomains.

T_m and ΔH are plotted against T_c in Fig. 2(**a**) for PVL-PS and PVL/PS with ϕ_{PVL} = 0.29. The values for the PVL homopolymers are significantly higher than those for the PVL blocks, suggesting that the chain confinement suppresses more favorable crystallization. The time evolution of ΔH is plotted for cylindrical (Fig. 2(**b**)) and spherical (2(**c**)) nanodomains. The initial crystallization rate of the PVL blocks is *ca.* 3 times larger than that of the PVL homopolymers, indicating the dominance of nucleation at the nanodomain interface. In summary, the crystallization of cylindrically and spherically confined PVL homopolymers as well as PVL blocks can be approximately described by *first-order kinetics*, but we can observe significant differences in their crystallization rates.

REFERENCES

[1] S. Nojima, M. Toei, S. Hara, S. Tanimoto and S. Sasaki, *Polymer*, **43** (2002) 4087.
[2] S. Nojima, Y. Ohguma, S. Namiki, T. Ishizone and K. Yamaguchi, *Macromolecules*, **41** (2008) 1915.

BEAMLINE

10C

S. Nojima[1], Y. Ohguma[1], S. Namiki[1], T. Ishizone[1] and K. Yamaguchi[2] ([1]Tokyo Inst. of Tech., [2]Kanagawa Univ.)